Temporal characteristics of groundwater chemistry affected by the 2016 Kumamoto earthquake using self-organizing maps

Kei Nakagawa*, Zhi-Qiang Yu, Ronny Berndtsson, Takahiro Hosono

Kei Nakagawa (✉)

Institute of Integrated Science and Technology, Nagasaki University,

e-mail: kei-naka@nagasaki-u.ac.jp

Tel.: +81 95 819 2763; fax: +81 95 819 2763

* corresponding author

Zhi-Qiang Yu

Graduate School of Fisheries and Environmental Sciences, Nagasaki University,

1-14 Bunkyo-machi, Nagasaki 852-8521, Japan

Ronny Berndtsson

Division of Water Resources Engineering & Center for Middle Eastern Studies, Lund University,

Box 118, SE-221 00 Lund, Sweden

Takahiro Hosono

Department of Earth and Environmental Science, Kumamoto University,

2-39-1 Kurokami, Kumamoto 860-8555, Japan

Abstract

Possibilities to perform pre- and post-seismic groundwater chemical comparisons on regional groundwater flow systems are rare due to lack of data and observations. The Kumamoto earthquake provides an unusual opportunity to improve the knowledge on earthquake hydrology and earthquake effects on hydrochemistry of groundwater due to a wealth of pre- and post-quake observations. We analyzed 12 physiochemical parameters (SiO_2, (NO_3^-+NO_2^-)-N, Fe_{total}, Mn_{total}, pH, F^-, Cl^-, SO_4^{2-}, Na^+, K^+, Ca^{2+}, and Mg^{2+}) using self-organizing maps (SOM) combined with hydrological and geological characteristics to improve the understanding of changes in groundwater chemistry after a major earthquake. The results indicate that the earthquake induced hydrological and environmental change via fault forming (Suizenji fault systems), liquefaction, rock fracturing, and ground shaking. These geological processes created rock fresh reactive surfaces, rock loosening, and enhancement of hydraulic conductivity. In turn, this lead to secondary processes in groundwater chemistry by advection, dilution, and chemical reaction. The most obvious indicator of hydrological and

environmental change was from the increased dissolved silica content stemming from fracturing and Si-O bond cleavage in silicate rocks. Besides this, decreasing concentration of common ions (Cl^-, F^-, Na^+, K^+, Ca^{2+}) was found due to dilution from mountain-side water release. Increase in (NO_3^-+NO_2^-)-N, SO_4^{2-}, and Mg^{2+} concentration occurred locally due to soil leaching of contaminants or agricultural fertilizers through surface ruptures in recharge areas. Increase of SO_4^{2-} content also originated from leaching of marine clay in coastal areas and possibly sporadic deep crustal fluid upwelling. Increase in (NO_3^-+NO_2^-)-N and Cl^- content occurred from sewage water pipe breaks in the Suizenji fault formation in urban areas. Decrease of pH occurred in a few wells due to mixing of river water and different types of aquifer groundwater. Increase of Fe_{total} and Mn_{total} concentration possibly originated from leaching of marine clay by liquefaction in coastal areas. However, in most cases the water chemistry changes were subtle, thus not resulting in any groundwater quality deterioration of water supplies.

Keywords: Kumamoto earthquake; Self-organizing maps; Groundwater geochemistry; Earthquake hydrology

1. Introduction

On 16 April 2016, a 7.0 Mw earthquake struck the Kumamoto area on Kyushu Island (southern

Japan), resulting in severe damage to infrastructure, buildings in the epicenter area, and more than 200 fatalities. A series of mainly three ≥5.5 Mw foreshocks and four >5.0 Mw aftershocks accompanied the main-shock within a week, forming the Kumamoto earthquake sequence. Its focal mechanism was a strike-slip movement of the active Hinagu-Futagawa faults and the largest inland earthquake on Kyushu Island since implementation of observations in 1885. It was a shallow earthquake with a focal depth of about 11 km (Japan Meteorological Agency, 2016; Lin, 2017; Hosono et al., 2018).

Crustal earthquakes induce large tectonic and crustal deformation such as surface ruptures, liquefaction, and mountain landslides in affected regions. Simultaneously, these geological structure deformations and ground shaking usually trigger hydrological and environmental phenomena. Such phenomena involve eruption of mud volcanoes, increased streamflow discharge, formation of new springs, depletion of existing springs, liquefaction, groundwater temperature variation, anomalous fluctuations in groundwater levels, and water chemical composition changes (Tsunogai and Wakita, 1996; Claesson et al., 2004; Cox et al., 2012; Shi et al., 2015; Wang and Manga, 2010, 2015; Rosen et al., 2018). Some of the first observations including well-documented earthquake precursors such as radon anomalies in deep groundwater were done at the Tashkent earthquake in 1966. Radon concentration, in several deep wells (depth of 1200~2400 m) in the affected areas, gradually increased and reached a maximum concentration at the precede of the earthquake (Ulomov and

Mavashev, 1971). Since then, groundwater chemistry variation prior to the earthquake has been suggested as an indicator for seismic prediction. In order to find scientific methods for earthquake forecasting, continuous monitoring of anomalous hydrological and hydro-geochemical response is necessary. Such studies include long-term monitoring of groundwater concentration change, water level variation characteristics, and frequent water sampling for hydro-geochemical analysis in sensitive seismic areas (Igarashi et al., 1995; Chia et al., 2001; Claesson et al., 2004; Koizumi et al., 2004; Skelton et al., 2014). Many studies have been devoted to pre-seismic and co-seismic hydrological phenomena such as groundwater physicochemical variables (e.g., dissolved ions, inert gas, isotope content, trace elements, EC, and pH) and anomalous water level variation to elucidate mechanical principles of occurring hydro-geochemical phenomena to further explore the possibility of earthquake precursors. The results of these efforts can be summarized as follows; 1) aquifer rupturing induces mixing of different aquifer groundwater in aquifer material strain and/or fracture zones, 2) ground and bedrock shaking causes rock loosening that facilitates release of partly stagnant fluids, 3) rock fractures give rise to increase of fresh rock reactive surfaces, and 4) earthquake-induced geological tectonic deformations release deep geothermal fluids into groundwater or springs (Thomas, 1988; Tsunogai and Wakita, 1996; Hartmann and Levy, 2005; Barberio et al., 2017; Paudel et al., 2018; Rosen et al., 2018).

Groundwater studies in the Kumamoto area are made using multiple techniques and

methods. Water supply for residents in the Kumamoto area is mainly from groundwater resources. Thus, high-resolution monitoring wells are used for ensuring safe water quality and quantity. Research in the area before the earthquake, has included a comprehensive regional hydrogeological and hydro-geochemical survey that has accumulated a wealth of hydrogeological background information and groundwater data (Hosono et al., 2013; Hosono et al., 2014; Kagabu et al., 2017). Most of the geochemical elements in the groundwater have been shown to be relatively stable during five years before the Kumamoto earthquake. Some groundwater constituents, however, such as nitrate and fluoride, have had an increasing trend due to anthropogenic activities (Hosono et al., 2013; Hossain et al., 2016a).

Reference studies are of vital significance for further insight into earthquake-related hydrological processes. Sano et al. (2016) studied links between co-seismic deep groundwater helium anomalies and earthquake-related geophysical tension changes in the earthquake area. They suggested that helium emission may be caused by rock fracturing in the seismic fault zone. Helium content was positively correlated with fault distance. By applying lab experiments to show the association between helium degassing and rock fracturing under compressive tension, the authors proposed that helium anomaly change in the seismic fault area may be a new approach for earthquake prediction (Sano et al., 2016). Hosono et al. (2018) interpreted earthquake-induced geological structural deformation using two kinds of hydrological phenomena in the active Aso

volcanic system. By numerical calculation and hydro-geochemical data analysis, they evaluated enhanced hydrothermal solute fluxes and mechanisms for new spring formations. Nakagawa et al. (2019) analyzed transient spatiotemporal variation in groundwater level characteristics in the study area using self-organizing maps (SOM). By a comparative analysis of water level change features for foreshock and main-shock, the authors concluded that spatial variation in groundwater levels is likely to be affected by local geophysical aquifer characteristics, earthquake magnitude, and hypocenter distance. Meanwhile, most of the unconfined aquifer wells (shallow wells with a depth of about 0~50 m) quickly recovered to initial water levels after several hours to a few days after the earthquake due to hydrostatic head. Most confined aquifer wells (deep wells at about 60~200 m) in the study area, however, need weeks to several months to recover to normal levels after an earthquake. Observation of these processes is crucial for a better understanding of earthquake effects associated with hydrological phenomena as well as for possible earthquake-prediction indicator use. Nakagawa et al. (2019) applied statistical methods to analyze groundwater level change affected by the earthquake. By analysis of the spatiotemporal distribution of groundwater level change after earthquake, an emergency water resources management practice was proposed (Nakagawa et al., 2019). However, this practice was suggested by only considering groundwater level changes (water quantity changes). Changes in water quality after earthquakes were not considered. Thus, in the present study, we explore observed groundwater chemical changes and try to link them to

earthquake-induced hydro-geochemical processes. Systematic studies of post-earthquake hydro-geochemical groundwater conditions are still very rare. The great magnitude of the Kumamoto earthquake together with a unique hydro-geochemical pre- and aftershock data collection provide an unusual opportunity to improve our knowledge on seismic effects on hydro-geochemistry. In this spirit, self-organizing maps (SOM) were applied to explore the complex spatiotemporal interactions of earthquake-induced hydro-geochemical changes in groundwater. The SOM helps to interpret similarity in complex spatiotemporal variation patterns not easily distinguished by traditional statistics. Similarly, the SOM together with cluster analysis are efficient in distinguishing between different groups of geochemical elements that can be systematically compared to different earthquake induced processes. According to this, concentration change ratios before and after the earthquake for 12 physicochemical variables were analyzed. The results are discussed in terms of changes in geophysical aquifer characteristics due to the earthquake. Finally, the robustness of the SOM analyses is discussed.

2. Study area

The Kumamoto groundwater aquifer is recharged from the Shirakawa and Midorikawa River Basins (**Fig. 1**). The two basins cover an area of 945 km^2. The aquifer is surrounded by the Aso Mountain (1592 MASL) in the east, the Ariake Sea and Kinpo Mountain (665 MASL) in the west, the

Midorikawa River in the south, and the Shirakawa River in the north. The groundwater is mainly recharged from the Aso Mountain area and three major highlands (Ueki, Kikuchi, and Takayubaru highland areas) together with surface water from the two rivers (Taniguichi et al., 2019). Subsequently, groundwater discharges from the lowlands into the Ariake Sea (Hosono et al., 2013; Hossain et al., 2016a). The geological features contain four main parts; 1) bedrock of Paleozoic metamorphic rock, Mesozoic granitic rock, and marine sediments, 2) pre-Aso volcanic rock from the Tertiary-Quaternary period, 3) Quaternary Aso volcanic rock, and 4) marine lacustrine deposits. Paleozoic and Mesozoic rock is the base bedrock with no outcrops in the study area. The pre-Aso volcanic rock is composed of lava and tuff breccia, constituting the Kinpo and Tatsuta mountains. Mount Aso volcanic rock is constituted by four main eruptions (Aso-1 (270 ka), Aso-2 (140 ka), Aso-3 (120 ka), and Aso-4 (89 ka)), constituting pyroclastic deposits as well as lava flows. A geological background map is shown in **Fig. 2**. Aso volcanic rock has great spatial extension in the study area and constitutes an important two-layer structured aquifer. The uppermost Aso-4 and partial alluvial deposits form a near-surface unconfined aquifer. The Aso-1, Aso-2, and Aso-3 have developed into a confined aquifer. The former aquifer thickness is uneven, from a few meters to 50 m depth, while the latter aquifer thickness ranges from 60-200 m below soil surface. Discontinuous alluvial deposits and marine sediments form an aquiclude between the unconfined and confined aquifers (Hosono et al., 2013; Hosono et al., 2014; Kagabu et al., 2017). In addition, a thick marine

clay from marine silt and sand bed of Shimabara Bay formation covers the unconfined aquifer in the coastal area (Hossain et al., 2016b). In tectonic terms, Kyushu Island is located on a subduction zone of tectonic plates, where the Philippine Sea plate is subducting below the Eurasian plate toward northwest. The average rate of plate convergence is about 7 cm per year (Seno et al., 1993). At the same time, the active Hinagu-Futagawa seismogenic fault zone is located on the western extension of the Median Tectonic Line throughout the Kumamoto area. Paleoseismic studies indicate that morphogenic crustal earthquakes (≥7 Mw) occur periodically in the active Hinagu-Futagawa fault zone. The periodic interval is about once a millennium (Chen et al., 2017; Lin et al., 2018). The recurrent crustal earthquakes, may induce major hydrological phenomena with a similar periodic occurrence. Examples of these may be new spring formations and depletion of previously existing springs near causative faults (Hosono et al., 2018).

The regional climate is subtropical humid. Average annual temperature and rainfall are approximately 16.9 ℃ and 1986 mm, respectively. About 40% of the annual precipitation stem from the summer monsoon during June and July (Japan Meteorological Agency, 2018).

3. Materials and methods

3.1 Self-organizing maps (SOM)

SOM is a kind of artificial neural network, which was originally developed by Kohonen (1982;

2001). SOM is a powerful and effective tool for complex data analyses such as classification, data mining, estimation, and prediction with unsupervised training. Consequently, SOM has been used in many disciplines (e.g., meteorology, hydrology, ecology, and groundwater) (e.g., Nishiyama et al., 2007; Kalteh et al., 2008; Bedoya et al., 2009; Nguyen et al., 2015; Nakagawa et al., 2017). Its main advantage is that it can project high-dimensional, complex target data into a low-dimensional array (usually two-dimensional), regular visualized map on the basis of data similarity characteristics (Jin et al., 2011; Nguyen et al., 2015). Using SOM, informative reference vectors are obtained via iterative updates under three main successive procedures, which is competition with nodes, selection of a winner node, and updating of the reference vectors (Choi et al., 2014; Yu et al., 2018). However, selection of proper initialization and data processing methods is extremely important before applying SOM. According to SOM properties, a larger map size enables obtaining a higher resolution pattern recognition. The optimum number of SOM nodes is decided by heuristic rule based on,

$$m = 5\sqrt{n} \tag{1}$$

where m stands for the number of SOM map nodes and n is the number of input data. The number of vertical and horizontal columns is based on the square root of the ratio between the two largest eigenvalues of transformed data. The eigenvalues are acquired from principal component analysis (Hilario and Ivan, 2004; Hentati et al., 2010; Nguyen et al., 2014).

Following the above general methodology, the SOM structure was determined.

Subsequently, the reference vector was obtained. The k-means algorithms are frequently applied for efficient clustering of SOM reference vectors (Jin et al., 2011). Davies-Bouldin Index (DBI) can be used to determine the optimal cluster number based on k-means algorithms. The calculation is in accordance with "similarity within a cluster" and "dissimilarity between cluster". After this, a fine-tuning cluster analysis was implemented by using Ward's method (Güler et al., 2002). The smallest DBI corresponds to an optimal number of clusters (Nguyen et al., 2015). More details on SOM can be found in Kohonen (1982; 2001), Vesanto et al. (2000), and Nakagawa et al. (2017). The above calculation steps were carried out applying a modified version of SOM Toolbox 2.0 (Vesanto et al., 2000).

3.2 Sampling and chemical analysis

Groundwater chemical data were obtained from two different administrative departments in Kumamoto (Kumamoto City and Kumamoto City Waterworks and Sewerage Bureau). The two departments sample groundwater from 35 and 132 wells, respectively. Kumamoto City carries out water sampling in June and October and Kumamoto City Waterworks and Sewerage Bureau performs water sampling in April, August, and November. Due to different measuring purposes and agendas of the two departments, observed variables and sampling dates are different between the two departments. Groundwater wells and chemical constituents were chosen so as to cover a

representative area of the groundwater aquifer and a maximum number of joint chemical constituents. After an initial analysis of available data, we found that most of the observed physiochemical parameters such as heavy metals and organic substances are continuously below the detection limit. Thus, 12 physiochemical parameters were selected as input vector for the SOM analysis due to observations by both departments and occurrence of regular non-zero values. These variables are dissolved silica (SiO_2), nitrate nitrogen ((NO_3^-+NO_2^-)-N), dissolved total iron (Fe_{total}), dissolved total manganese (Mn_{total}), pH, Fluoride (F^-), chloride (Cl^-), sulfate (SO_4^{2-}), sodium (Na^+), potassium (K^+), calcium (Ca^{2+}), magnesium (Mg^{2+}). These observations come from 67 groundwater wells (**Fig. 1**; Aster Global DEM V2 from earth data of NASA (http://gdex.cr.usgs.gov/gdex/)). Well characteristics (well depth, screen depth, and aquifer type) are summarized in **Table 1**. Other well information (size, water level, and hydrogeological parameters) is described in the supporting information of Hosono et al. (2019). Similar to Hosono and Masaki (2020), we estimated long-term normal concentration for 2016 (pre-earthquake) by linear regression and data from 2011 to 2015. A concentration ratio was calculated by dividing concentration just after the earthquake by estimated concentration using 5-year data before the earthquake:

$$\text{concentration ratio} = \frac{\text{measured concentration in 2016}}{\text{estimated concentration in 2016 based on 5-year data before earthquake}} \quad (2)$$

The concentration ratio was used as input to the SOM calculations to evaluate the earthquake-induced effects on the groundwater chemistry. If ion concentration was zero, the

concentration ratio of the sample was set to zero. Reference vectors from the SOM analysis were divided into groups by use of cluster analysis with k-means and Ward's algorithms. Radar charts for each cluster were used to analyze the extent of the earthquake on the 12 investigated groundwater chemicals. A general criterion that was used to analyze effects of the earthquake is the ±2 times of standard deviation plus the estimated concentration. This criterion defined the upper limit and lower limit of groundwater chemistry fluctuation caused by the earthquake. If concentration fluctuated within the range of this threshold, it is interpreted as normal variation. The opposite case is interpreted as an earthquake-induced change (Claesson et al., 2004; Skelton et al., 2014; Hosono and Masaki, 2020).

4. Results and discussion

4.1 SOM and clustering analysis

Concentration ratios of the 12 physiochemical variables (SiO_2, (NO_3^-+NO_2^-)-N, Fe_{total}, Mn_{total}, pH, F^-, Cl^-, SO_4^{2-}, Na^+, K^+, Ca^{2+}, and Mg^{2+}) for the 67 sampling locations was used as input to the SOM calculations. The number of SOM node reference vectors was calculated to 42, with 7 vertical and 6 horizontal columns. SOM maps for the 12 variables after training are shown in **Fig. 3**. Every map represents a component value for the 42 reference vectors, where vectors have been standardized into the range 0-1. Thus, if the node color is red, it means a relatively high concentration ratio, while

a blue color represents relatively low concentration ratio. In general, Fe_{total}, Mn_{total}, Mg^{2+}, and SO_4^{2-} displayed relatively blue color maps. These parameters were generally not affected by the earthquake. On the contrary, in the maps for $(NO_3^-+NO_2^-)$-N, Cl^-, Na^+, and K^+, red neurons stand out. This means that these chemical parameters were affected by the earthquake. Maps of Fe_{total} and Mn_{total}, Na^+, K^+ and Cl^-, Mg^{2+} and SO_4^{2-} show great similarity. Accordingly, these groups of chemicals seem to have same mechanism of concentration change by the earthquake effect.

DBI variation is shown in **Fig. 4** and a minimum DBI is obtained for a cluster number equal to 6. Consequently, a hierarchical clustering algorithm according to Ward's method (Güler et al., 2002) was implemented for 6 clusters (**Fig. 5**). From **Fig. 5**, it is seen that out of the 6 clusters, 4 and 6 are close and thus, they have a high similarity. Likewise, 2 and 5, and 1 and 3 are as well similar.

The pattern classification map for the 6 clusters is displayed in **Fig. 6**. In the figure, well numbers have been included. Each cluster manifests specific groundwater chemistry characteristics. For example, cluster 1 is characterized by relatively high concentration ratios for $(NO_3^-+NO_2^-)$-N, SiO_2, and pH. On the contrary, the concentration ratios for Fe_{total}, F^-, Cl^-, SO_4^{2-}, Na^+, K^+, Ca^{2+}, and Mg^{2+} are comparatively low. These features are observed in corresponding locations of each SOM component map in **Fig. 3**.

4.2 Changes in groundwater chemistry

In order to facilitate the interpretation of earthquake-induced effects on groundwater chemistry, radar charts are used with information from **Table 2**. The general chemical characteristics of each cluster in the radar charts are shown as first quartile, median, and third quartile. The red unit circle in the charts serves as reference for each cluster. Characteristics of groundwater chemistry for the 6 clusters are shown in **Fig. 7**. The figure is based on raw input data to the SOM (no standardization) to evaluate actual fluctuations of the concentration ratios. Each radar chart as well, includes the total number of wells that have been included. Concentration ratios close to 1 are interpreted as negligible effects from the earthquake. For other chemical variables, such as $(NO_3^-+NO_2^-)$-N, Mn_{total}, Fe_{total}, and F^-, concentration ratios may be close to 0 due to very small concentration in the groundwater sample.

Cluster 1 displays relatively high concentration ratio for SiO_2 and $(NO_3^-+NO_2^-)$-N. The first quartile values are in the range ≥1, but with relatively low concentration ratios for Mn_{total}, F^-, Cl^-, Na^+, K^+, and Ca^{2+}. As well, the third quartile values are ≤1. Thus, median values for pH, SO_4^{2-}, Mg^{2+} are more or less superimposed onto the unit circle. Median value for Fe_{total} is close to 0.

Cluster 2 displays a similar general pattern as cluster 1. Smaller concentration ratios are at hand for SiO_2 and $(NO_3^-+NO_2^-)$-N, as well as relatively small ratios for F^-. For the third quartile, F^- is lower than 1. The concentration ratios for Fe_{total} and Mn_{total} are close to 0. Other chemicals (pH, Cl^-,

SO_4^{2-}, Na^+, K^+, Ca^{2+}, and Mg^{2+}) are basically overlapping the unit circle. This is interpreted as very small effect of the earthquake on the groundwater chemistry.

Cluster 3 is characterized by higher concentration ratios for Fe_{total}, Mn_{total}, F^-, and SiO_2. The first quartile values for Fe_{total}, Mn_{total}, and F^- are larger than 1. The (NO_3^-+NO_2^-)-N is close to 0. pH and Na^+ are close to the unit circle. However, median values for other parameters (Cl^-, SO_4^{2-}, K^+, Ca^{2+}, and Mg^{2+}) are less than the unit circle. The fluctuation of Fe_{total}, Mn_{total} and SO_4^{2-} are comparatively larger.

Clusters 4 and 6 only have 2 and 3 water samples in each cluster, respectively. These wells will be discussed in detail below.

Cluster 5 has higher concentration ratio for SiO_2, SO_4^{2-}, and (NO_3^-+NO_2^-)-N. The first quartile values are larger than 1. The concentration ratios of Cl^-, pH, Na^+, K^+, Ca^{2+}, and Mg^{2+} are basically stable onto the unit circle. Other variables like Fe_{total}, Mn_{total}, and F^- are close to 0.

All data that have clearly been affected the earthquake are summarized in **Table 2** for each cluster. Cluster 1 includes 12 wells. SiO_2 and (NO_3^-+NO_2^-)-N concentration increased in 8 and 3, wells, respectively. Concentrations of F^-, Cl^-, Na^+, K^+, and Ca^{2+} were low but noticeable in 4, 7, 3, 1, and 3 wells, respectively. pH fluctuated in the range of natural variability. Fe_{total}, Mn_{total}, SO_4^{2-}, and Mg^{2+} concentrations were sporadically smaller or larger. These features are generally consistent with the overall tendency of radar charts and SOM maps. These results are likely related to the earthquake

induced large-scale surface ruptures (**Fig. 8**), rock fractures, and ground shaking of the groundwater recharge area of the Aso-mountain chains. At the same time, some of the wells of Cluster 1 are located in an agricultural area. Human agricultural activity leads to large-scale and long-term nitrate transport during pre-earthquake (Hosono et al., 2013; Fujiwara et al., 2016). Results from bond cleavage fracture in silicate rocks are Si-O dissolution into groundwater, and increased soil nitrate transport into groundwater through new pathways and permeability enhancement due to the earthquake. These processes increase the silicate dissolution and constitute a part of the nitrate nitrogen increase. At the same time, the pre-earthquake groundwater flow paths are disturbed, and the water-rock interactions through new fresh rock reactive surfaces influence the ion dissolution (SO_4^{2-}, Na^+, K^+, Ca^{2+}, and Mg^{2+}). Mountainside water transport, however, dilutes most of the well water in recharge areas. The process of permeability enhancement due to new soil and rock cracks cause mountainside water dilution affecting the recharge areas and groundwater levels (GWL) and TDS. This is shown by the increasing GWL by several meters for most of the wells, noticeable even one year after the earthquake. Thus, mountainside water will dilute original groundwater and display a decreasing TDS (Hosono et al., 2019; Hosono and Masaki, 2020).

Cluster 2 covers 33 wells. Increasing SiO_2, $(NO_3^-+NO_2^-)$-N, Cl^-, SO_4^{2-}, and Mg^{2+} concentrations were found in 13, 10, 8, 6, and 4 wells, respectively. The F^- concentration decreased in 17 wells. Fe_{total}, Mn_{total}, Ca^{2+} concentrations and pH changed in some of the wells. The Na^+ and K^+

were relatively unaffected in all 33 wells. As above, a likely reason is mineral dissolution of fresh rock reactive surfaces, water-rock interactions, and agricultural fertilizers seeping into groundwater via permeability enhancement and new rupture pathways in agricultural areas. These changes can explain a part of the increasing SiO_2, $(NO_3^-+NO_2^-)$-N, and SO_4^{2-} concentration. In addition, wells in cluster 2 are located in urban areas (**Fig. 8**). The earthquake formed a new Suizenji fault system, and broke sewer pipes resulting in sewage water leakage to the groundwater. This is a probable cause for increase in nitrate and chloride concentrations (Hosono et al., 2019). Sporadic increase in SO_4^{2-} and Cl^-concentrations probably originates from deep crustal fluid upwelling during formation of new fault areas. This phenomenon is indicated by anomalous change of other trace elements such as boron, because deep hydrothermal fluids enrich sulfate, chloride, and boron elements to the groundwater (Hosono et al., 2018).

Cluster 3 includes 6 wells. An increase in Fe_{total}, Mn_{total}, SiO_2, and F^- was noted for 4, 2, 2, and 1 well, respectively. In particular, a sharp decrease of Cl^- and Na^+ occurred in 2 and 1 well, respectively. pH, SO_4^{2-}, and K^+ changed in specific wells. Ca^{2+}, Mg^{2+}, and $(NO_3^-+NO_2^-)$-N (original concentration is 0) were not influenced by the earthquake. Usually stable ratios of Cl^- and Na^+ changed significantly in one specific well (T20) close to the coast. The main reason for this is triggering of liquefaction in the coastal area. This leads to lower concentration due to groundwater upwelling and water mixing in the original aquifer. This well likely also to be affected by aquifer

breaching through liquefaction. At the same time, the strata of unwashed marine clay sediments are broken by the earthquake and new fracture ruptures are leached by new groundwater flow. The Ariake clay is enriched by Fe and Mn oxides/hydroxides causing this process to give rise to increasing concentrations of Fe_{total} and Mn_{total}. This is noted by a groundwater chemistry change that continues over several months. In addition, the degree of water chemistry change is different for similar locations (T20 and T21) (**Fig. 8**). The reason for this likely different well depths (100 and 15 m, respectively). This results in a different mixture ratio for fluids at the different well depths.

Cluster 4 includes two wells. Water samples from T35 display increased Fe_{total} and Mg^{2+} concentrations. pH was clearly less than the lower limit (estimated concentration –2σ). Other chemical variables were less influenced by the earthquake. With many new fault surfaces along the riverside area, surface water was mixed with groundwater, thus causing a water quality change. This phenomenon is also shown by the variation of river water level and total dissolved carbon. Observation of river water levels near the T35 well, showed a decline after the main earthquake. This is due to that the new Suizenji fault system triggered massive flow of surface water to the groundwater (Hosono et al., 2019). In addition, the total dissolved carbon of groundwater at T35 increased from less than 0.1 to 0.3 mg/L as compared to before the earthquake. The origin of total dissolved carbon is surface soil material that was transported through the new ruptures deep into the groundwater (Hosono and Masaki, 2020).

Cluster 5 includes 11 wells. SiO_2, SO_4^{2-}, and Mg^{2+} tended to exceed the upper limit in 9, 4, and 2 wells, respectively. Cl^- concentration was small in 3 of 11 wells. $(NO_3^-+NO_2^-)$-N and Ca^{2+} indicate small influence in some wells. Other parameters (Fe_{total}, Mn_{total}, pH, F^-, Na^+, and K^+) were in the range of natural variability. At most of the sampling locations in the recharge area, the main causes of groundwater chemistry change are rock fracture dissolution, mountainside water dilution, and possible sources of SO_4^{2-} and Mg^{2+} from agricultural fertilizer infiltration.

Finally, Cluster 6 includes 3 wells. Increased ratios for SO_4^{2-} occurred in all 3 wells. Besides, T52 displayed a small increase in concentration for F^- and Mg^{2+}. Other variables were basically unchanged. There are massive volumes of unwashed marine clay sediments distributed in the stagnant groundwater area of the coastal zone, earthquake-induced liquefaction leached and/or released stagnant groundwater through these newly formed fractures. The result is a possible release of SO_4^{2-} of marine origin into the groundwater.

In order to explore water chemistry characteristics before the earthquake, we calculated estimated concentrations for 2015 using five year's data (from 2010 to 2014 year). Then, the concentration ratios between actual and estimated 2015 concentration were calculated and fed into the SOM for analysis. The cluster results indicate that the 67 wells can be classified into six clusters (**Fig. 9**), just as in the previous analysis. The results should accordingly reflect close to normal conditions (without effects of the earthquake). We regard the outcome as a description of almost

natural conditions and this is very different from the spatiotemporal characteristics after the earthquake as compared to the above. Thus, the earthquake indicates a radical change in spatiotemporal water quality characteristics.

A comparison of the corresponding radar chart maps (**Fig. 7** compared to radar chart maps for almost normal condition as above (**Fig. 10**)) shows that each of the six clusters have changed after the earthquake. The most important properties are that concentrations for SiO_2, Fe_{total}, Mn_{total}, pH, Cl^-, SO_4^{2-}, Na^+, K^+, Ca^{2+}, and Mg^{2+} are all relatively stable in groundwater before the earthquake. They basically fluctuate in the range of ±2σ of the estimated concentrations. Sporadic water samples exceed this general variation. In recent years, the concentration of $(NO_3^-+NO_2^-)$-N and F^- has gradually increased due to environmental factors and some well water exceeded ±2σ variation even before the earthquake. The general methodology adopted in this paper can be said to be efficient in comparing almost normal to major effects of an earthquake.

5. Conclusions

In this study, groundwater chemistry was examined after a major earthquake by the use of SOM analysis. The general change of chemical characteristics of the groundwater as shown in the radar chart for each cluster is basically consistent with the results of a quantitative analysis for respective cluster as shown in **Table 2**.

Cluster 1 included 12 wells. These are mainly distributed over upstream recharge areas for groundwater. The earthquake increased the concentration of SiO_2 and $(NO_3^-+NO_2^-)$-N and decreased the concentration of F^-, Cl^-, Na^+, K^+, and Ca^{2+}. Other parameters were not affected. The mechanisms of earthquake-induced groundwater chemistry change are massive triggering of surface ruptures, rock fractures, and ground shaking. This creates fresh reactive rock surfaces and permeability enhancement through the ruptures and fractures. This process increases dissolved silicates as well as nitrate-nitrogen concentration. In addition, released mountainside water dilutes the contents of F^-, Cl^-, Na^+, K^+, and Ca^{2+}.

Cluster 2 contained 33 wells. The earthquake increased the concentration of SiO_2, $(NO_3^-+NO_2^-)$-N, Cl^-, SO_4^{2-}, and Mg^{2+}. However, F^- concentration decreased. Concentration changes and earthquake mechanisms for groundwater chemistry changes display similarities with Cluster 1. The main difference is that Cluster 2 is located in urban areas. Thus, the earthquake destroyed sewer pipes through the new Suizenji fault system. This meant that sewage water leaked into the groundwater, increasing nitrate and chloride concentrations. The increase in SO_4^{2-} and Mg^{2+}concentration is likely an effect of agricultural fertilizers seeping into the groundwater through new pathways. Possibly, deep crustal upwelling of fluids may also give rise to increasing SO_4^{2-} and Cl^- concentrations.

Cluster 3 included 6 wells. These displayed increasing Fe_{total}, Mn_{total}, and SiO_2 and sharp

decrease of Cl^- and Na^+ concentration. pH, SO_4^{2-}, and K^+ were influenced at specific wells. Cluster 3 wells are mainly located in coastal areas. The earthquake gives rise to liquefaction and aquifer breaching resulting in a mixing of groundwater from different aquifer systems. In addition, the earthquake leads to new seismic fractures for the strata of unwashed marine clay sediments and leaching of groundwater. These processes are likely to increase Fe_{total} and Mn_{total} concentration.

Cluster 4 included 2 wells. Fe_{total} and Mg^{2+} displayed increasing concentration and pH decreased. The two wells are located along a riverside area. Thus, seismic effects are likely to increase surface water transport the groundwater through newly formed faults and ruptures. This has probably caused the observed water chemistry change.

Cluster 5 contained 11 wells. SiO_2, SO_4^{2-}, and Mg^{2+} concentration increased and Cl^- concentration decreased. $(NO_3^-+NO_2^-)$-N and Ca^{2+} were influenced in some of the wells. Cluster 5 wells are mainly located in recharge areas, and main mechanisms are similar to those of Cluster 1. These mechanisms are constituted by rock fracturing and mountainside water release leading to increasing dissolved silicates and decreasing Cl^- concentration. The increasing SO_4^{2-} and Mg^{2+}concentration may originate from infiltration of agricultural fertilizers.

Cluster 6 contained 3 wells. SO_4^{2-}, F^-, and Mg^{2+} increased. Other chemicals were basically unchanged. Cluster 6 is located in a coastal stagnant area. Possible reasons for observed increase in the above constituent concentrations are earthquake-induced liquefaction and release of marine

origin SO_4^{2-} through newly formed fractures and fissures.

In general, SOM can distinguish between complex spatiotemporal patterns in an efficient manner. In this case, however, it is obvious that the earthquake had great effects on average hydro-geochemical levels. Even so, SOM can help to interpret similarity in variation patterns not easily distinguished by traditional statistics. Similarly, the SOM together with cluster analysis are efficient in distinguishing between different groups of geochemical elements that can be systematically compared to quantitative water characteristics. SOM is, however, as all methods dependent on input data quality. Thus, input data need to be carefully preprocessed and quality checked. SOM results in a regular visual map on the basis of input data similarity. Meanwhile, according to the results of cluster analysis, we can combine with exploring the spatiotemporal characteristics of water chemistry change and local geological and hydrogeological background information.

According to the above, groundwater chemistry features from the cluster analysis can provide a water resources utilization plan for emergency conditions. For example, the nitrate-nitrogen content of Cluster 1 and 2 indicate increasing concentrations for wells in certain areas, due to leakage of agricultural fertilizers and sewage water. These wells need to be temporally discontinued for utilization. Other clusters (3, 4, 5, and 6) indicate wells that can be exploited even after an earthquake.

Acknowledgements This work was supported by JSPS KAKENHI under Grant No.JP17H01861 and SUNTORY Kumamoto groundwater research project for financial support.

References

Barberio, M.D., Barbieri, M., Billi, A., Doglioni, C., Petitta, M., 2017. Hydrogeochemical changes before and during the 2016 Amatrice-Norcia seismic sequence (central Italy). Sci. Rep. 7, 1–12. https://doi.org/10.1038/s41598-017-11990-8

Bedoya, D., Novotny, V., Manolakos, E.S., 2009. Instream and offstream environmental conditions and stream biotic integrity. Importance of scale and site similarities for learning and prediction. Ecol. Modell. 220, 2393–2406. https://doi.org/10.1016/j.ecolmodel.2009.06.017

Chen, P., Sado, K., Takahashi, N., Lin, A., Hirata, S., Satsukawa, T., 2017. Millennium Recurrence Interval of Morphogenic Earthquakes on the Seismogenic Fault Zone That Triggered the 2016 Mw 7.1 Kumamoto Earthquake, Southwest Japan. Bull. Seismol. Soc. Am. 107, 2687–2702. https://doi.org/10.1785/0120170149

Chia, Y., Wang, Y.S., Chiu, J.J., Liu, C.W., 2001. Changes of groundwater level due to the 1999 Chi-Chi earthquake in the Choshui River alluvial fan in Taiwan. Bull. Seismol. Soc. Am.

91, 1062–1068. https://doi.org/10.1785/0120000726

Choi, B.Y., Yun, S.T., Kim, K.H., Kim, J.W., Kim, H.M., Koh, Y.K., 2014. Hydrogeochemical interpretation of South Korean groundwater monitoring data using Self-Organizing Maps. J. Geochemical Explor. 137, 73–84. https://doi.org/10.1016/j.gexplo.2013.12.001

Claesson, L., Skelton, A., Graham, C., Dietl, C., Mörth, M., Torssander, P., Kockum, I., 2004. Hydrogeochemical changes before and after a major earthquake. Geology 32, 641–644. https://doi.org/10.1130/G20542.1

Cox, S., Rutter, H., Sims, A., Manga, M., Weir, J., Ezzy, T., White, P., Horton, T., Scott, D., 2012. Hydrological effects of the M W 7.1 Darfield (Canterbury) earthquake, 4 September 2010, New Zealand. New Zeal. J. Geol. Geophys. 55, 231–247. https://doi.org/10.1080/00288306.2012.680474

Fujiwara, S., Yarai, H., Kobayashi, T., Morishita, Y., Nakano, T., Miyahara, B., 2016. Small - displacement linear surface ruptures of the 2016 Kumamoto earthquake sequence detected by ALOS - 2 SAR interferometry. Earth, Planets Sp. https://doi.org/10.1186/s40623-016-0534-x

Güler, C., Thyne, G.D., McCray, J.E., Turner, A.K., 2002. Evaluation of graphical and multivariate statistical methods for classification of water chemistry data. Hydrogeol. J. 10, 455–474.

https://doi.org/10.1007/s10040-002-0196-6

Hartmann, J., Levy, J.K., 2005. Hydrogeological and gasgeochemical earthquake precursors – A review for application. Nat. Hazards 34, 279–304. https://doi.org/10.1007/s11069-004-2072-2

Hentati, A., Kawamura, A., Amaguchi, H., Iseri, Y., 2010. Evaluation of sedimentation vulnerability at small hillside reservoirs in the semi-arid region of Tunisia using the Self-Organizing Map. Geomorphology 122, 56–64. https://doi.org/10.1016/j.geomorph.2010.05.013

Hilario, L.G., and Ivan, M.G., 2004. Self-Organizing Map and Clustering for Wastewater Treatment Monitoring. Engineering Applications of Artificial Intelligence. 17, 215-225. http://dx.doi.org/10.1016/j.engappai.2004.03.004

Hosono, T., Hartmann, J., Louvat, P., Amann, T., Washington, K.E., West, A.J., Okamura, K., Böttcher, M.E., Gaillardet, J., 2018. Earthquake-induced structural deformations enhance long-term solute fluxes from active volcanic systems. Sci. Rep. 8, 14809. https://doi.org/10.1038/s41598-018-32735-1

Hosono, T., Tokunaga, T., Kagabu, M., Nakata, H., Orishikida, T., Lin, I.T., Shimada, J., 2013. The use of δ15N and δ18O tracers with an understanding of groundwater flow dynamics for evaluating the origins and attenuation mechanisms of nitrate pollution. Water Res. 47, 2661–2675. https://doi.org/10.1016/j.watres.2013.02.020

Hosono, T., Tokunaga, T., Tsushima, A., Shimada, J., 2014. Combined use of δ13C, δ15N, and δ34S tracers to study anaerobic bacterial processes in groundwater flow systems. Water Res. 54, 284–296. https://doi.org/10.1016/j.watres.2014.02.005

Hosono, T., Yamada, C., Shibata, T., Tawara, Y., Wang, C. - Y., Manga, M., Rahman, A.T.M.S., Shimada, J., 2019. Coseismic groundwater drawdown along crustal ruptures during the 2016 M_w 7.0 Kumamoto earthquake. Water Resour. Res. 2019WR024871. https://doi.org/10.1029/2019WR024871

Hosono, T., Masaki, Y., 2020. Post-seismic hydrochemical changes in regional groundwater flow systems in response to the 2016 Mw 7.0 Kumamoto earthquake. J. Hydrol. 580, 124340. https://doi.org/10.1016/j.jhydrol.2019.124340

Hossain, S., Hosono, T., Yang, H., Shimada, J., 2016a. Geochemical Processes Controlling Fluoride Enrichment in Groundwater at the Western Part of Kumamoto Area, Japan. Water. Air. Soil Pollut. 227. https://doi.org/10.1007/s11270-016-3089-3

Hossain, S., Hosono, T., Ide, K., Matsunaga, M., Shimada, J., 2016b. Redox processes and occurrence of arsenic in a volcanic aquifer system of Kumamoto Area, Japan. Environ. Earth Sci. 75, 1–19. https://doi.org/10.1007/s12665-016-5557-x

Igarashi, G., Saeki, S., Takahata, N., Sumikawa, K., Tasaka, S., Sasaki, Y., Takahashi, M., Sano, Y.,

1995. Ground-water radon anomaly before the Kobe earthquake in Japan. Science. 269, 60–61. https://doi.org/10.1126/science.269.5220.60

Japan Meteorological Agency, 2016. Report on the Heisei 28 (2016) Kumamoto earthquake (No. 10). http://www.jma.go. jp/jma/press/1604/16g/201604161530.html. Accessed 20 Dec 2016.

Japan Meteorological Agency, 2018. Weather observation data. Japan Meteorological Agency Web. http://www.jma.go.jp/jma/index.html. Accessed 16 November 2018

Jin, Y.H., Kawamura, A., Park, S.C., Nakagawa, N., Amaguchi, H., Olsson, J., 2011. Spatiotemporal classification of environmental monitoring data in the Yeongsan River basin, Korea, using self-organizing maps. Journal of Environmental Monitoring 13(10), 2886-2894. https://doi.org/10.1039/C1EM10132C

Kagabu, M., Matsunaga, M., Ide, K., Momoshima, N., Shimada, J., 2017. Groundwater age determination using85Kr and multiple age tracers (SF6, CFCs, and3H) to elucidate regional groundwater flow systems. J. Hydrol. Reg. Stud. 12, 165–180. https://doi.org/10.1016/j.ejrh.2017.05.003

Kalteh, A.M., Hjorth, P., Berndtsson, R., 2008. Review of the self-organizing map (SOM) approach in water resources: Analysis, modelling and application. Environ. Model. Softw. 23, 835–845. https://doi.org/10.1016/j.envsoft.2007.10.001

Kohonen, T., 1982. Self-organized formation of topologically correct feature maps. Biological Cybernetics 43(1): 59-69. https://doi.org/10.1007/BF00337288

Kohonen, T., 2001. Self-organizing maps, third ed. Springer, Berlin.

Koizumi, N., Kitagawa, Y., Matsumoto, N., Takahashi, M., Sato, T., Kamigaichi, O., Nakamura, K., 2004. Preseismic groundwater level changes induced by crustal deformations related to earthquake swarms off the east coast of Izu Peninsula, Japan. Geophys. Res. Lett. 31, 1–5. https://doi.org/10.1029/2004GL019557

Lin, A., 2017. Structural features and seismotectonic implications of coseismic surface ruptures produced by the 2016 Mw7.1 Kumamoto earthquake. J. Seismol. 21, 1079–1100. https://doi.org/10.1007/s10950-017-9653-5

Lin, A., Chen, P., Sado, K., 2018. Recurrent large earthquakes related with an active fault-volcano system, southwest Japan. Sci. Rep. 8, 1–10. https://doi.org/10.1038/s41598-018-32140-8

Manga, M., Wang, C.Y., 2015. Earthquake Hydrology, Treatise on Geophysics: Second Edition. Elsevier B.V. https://doi.org/10.1016/B978-0-444-53802-4.00082-8

Nakagawa, K., Amano, H., Kawamura, A., Berndtsson, R., 2017. Classification of groundwater chemistry in Shimabara, using self-organizing maps. Hydrology Research 48(3), 840-850. https://doi.org/10.2166/nh.2016.072

Nakagawa, K., Yu, Z.Q., Berndtsson, R., Kagabu, M., 2019. Analysis of earthquake-induced groundwater level change using self-organizing maps. Environ. Earth Sci. 78, 455. https://doi.org/10.1007/s12665-019-8473-z

Nguyen, T.T., Kawamura, A., Tong, T.N., Nakagawa, N., Amaguchi, H., Gilbuena, R., 2014. Spatial classification of groundwater monitoring data in the Red River Delta, Vietnam using self-organizing maps. Annual Journal of Hydraulic Engineering, JSCE 70(4), I_241-I_246.

Nguyen, T.T., Kawamura, A., Tong, T.N., Nakagawa, N., Amaguchi, H., Gilbuena, R., 2015. Clustering spatio-seasonal hydrogeochemical data using self-organizing maps for groundwater quality assessment in the Red River Delta, Vietnam. J. Hydrol. 522, 661–673.
https://doi.org/10.1016/j.jhydrol.2015.01.023

Nishiyama, K., Endo, S., Jinno, K., Bertacchi Uvo, C., Olsson, J., Berndtsson, R., 2007. Identification of typical synoptic patterns causing heavy rainfall in the rainy season in Japan by a Self-Organizing Map. Atmos. Res. 83, 185–200. https://doi.org/10.1016/j.atmosres.2005.10.015

Taniguchi, M., Burnett, K.M., Shimada, J., Hosono, T., Wada, C.A., Ide, K., 2019. Recovery of Lost Nexus Synergy via Payment for Environmental Services in Kumamoto, Japan. Front. Environ. Sci. 7, 1–8. https://doi.org/10.3389/fenvs.2019.00028

Paudel, S.R., Banjara, S.P., Wagle, A., Freund, F.T., 2018. Earthquake chemical precursors in groundwater: a review. J. Seismol. 22, 1293–1314. https://doi.org/10.1007/s10950-018-9739-8

Rosen, M.R., Binda, G., Archer, C., Pozzi, A., Michetti, A.M., Noble, P.J., 2018. Mechanisms of Earthquake-Induced Chemical and Fluid Transport to Carbonate Groundwater Springs After Earthquakes. Water Resour. Res. 54, 5225–5244. https://doi.org/10.1029/2017WR022097

Sano, Y., Takahata, N., Kagoshima, T., Shibata, T., Onoue, T., Zhao, D., 2016. Groundwater helium anomaly reflects strain change during the 2016 Kumamoto earthquake in Southwest Japan. Sci. Rep. 6, 1–7. https://doi.org/10.1038/srep37939

Seno, T., Stein, S., Gripp, A.E., 1993. A model for the motion of the Philippine Sea Plate consistent with NUVEL-1 and geological data. J. Geophys. Res. 98, 941–948. https://doi.org/10.1029/93JB00782

Shi, Z., Wang, G., Manga, M., Wang, C.Y., 2015. Mechanism of co-seismic water level change

following four great earthquakes - insights from co-seismic responses throughout the Chinese mainland. Earth Planet. Sci. Lett. 430, 66–74. https://doi.org/10.1016/j.epsl.2015.08.012

Skelton, A., Andrén, M., Kristmannsdóttir, H., Stockmann, G., Mörth, C.M., Sveinbjörnsdóttir, Á., Jónsson, S., Sturkell, E., Gudrúnardóttir, H.R., Hjartarson, H., Siegmund, H., Kockum, I., 2014. Changes in groundwater chemistry before two consecutive earthquakes in Iceland. Nat. Geosci. 7, 752–756. https://doi.org/10.1038/NGEO2250

Vesanto, J., Himberg, J., Alhoniemi, E., Parhankangas. J., 2000. SOM Toolbox for Matlab 5, Helsinki University of Technology Report A57.

Thomas, D., 1988. Geochemical precursors to seismic activity. Pure Appl. Geophys. 126, 241–266. https://doi.org/10.1007/BF00878998

Tsunogai, U., Wakita, H., 1996. Anomalous Changes in Groundwater Chemistry. Possible Precursors of the 1995 Hyogo-ken Nanbu Earthquake, Japan. J. Phys. Earth 44, 381–390. https://doi.org/10.4294/jpe1952.44.381

Ulomov, V.I., Mavashev, B.Z., 1971. Forerunners of the Tashkent earthquake. Izvestia Akadamiya Nauk Uzbekistan SSR, PP, 188-200.

Wang, C.Y., Manga, M., 2010. Hydrologic Responses to Earthquakes and a General Metric. Front. Geofluids 206–216. https://doi.org/10.1002/9781444394900.ch14

Yu, Z.Q., Amano, H., Nakagawa, K., Berndtsson, R., 2018. Hydrogeochemical evolution of groundwater in a Quaternary sediment and Cretaceous sandstone unconfined aquifer in Northwestern China. Environ. Earth Sci. 77, 629. https://doi.org/10.1007/s12665-018-7816-5

Figure & Table Captions

Figure 1 Study area with location of sampled wells (three highlands are the recharge areas of groundwater, existing a mass of Ariake clay sediments at coastal area is groundwater stagnant area).

Figure 2 Geological map of Kumamoto area (Ariake clay sediments are mainly

distributed at the dotted line (5 MASL) range of coastal regions).

Figure 3 SOM component planes for 12 physicochemical variables.

Figure 4 DBI as a function of number of clusters.

Figure 5 Dendrogram with cluster numbers.

Figure 6 Pattern classification map for 6 clusters based on SOM.

Figure 7 Radar charts for the 6 clusters in Fig. 6 (number of wells indicated at upper left corner of each chart).

Figure 8 Spatial distribution of 6 clusters in Fig. 7.

Figure 9 Pattern classification map for 6 clusters based on SOM (before earthquake).

Figure 10 Radar charts for the 6 clusters in Fig. 9 (before earthquake).

Table 1 Characterization of sampled wells.

Table 2 Data for earthquake-induced water chemistry anomaly based on each cluster.

Figure 1

Click here to download high resolution image

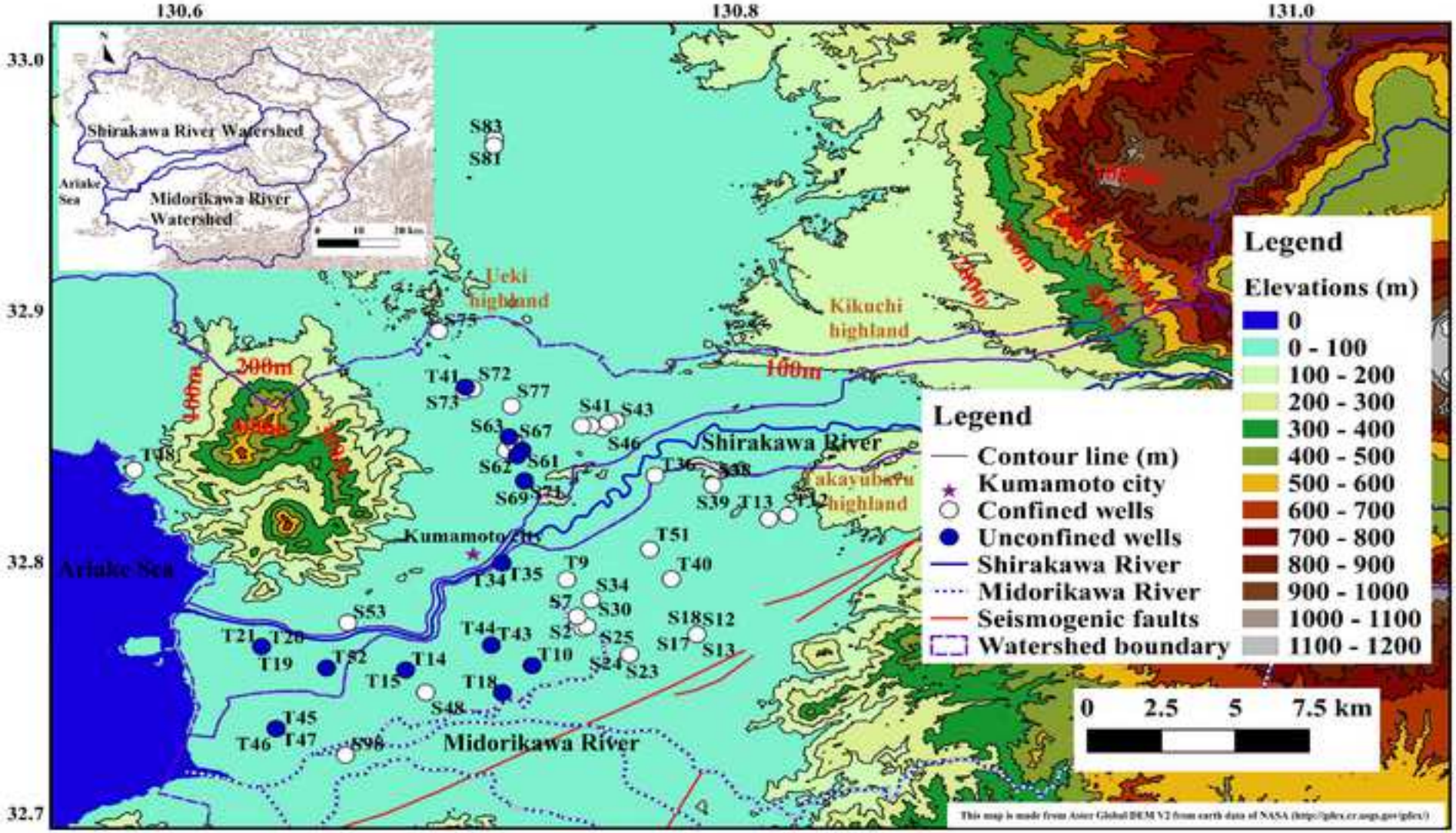

Figure 2
Click here to download high resolution image

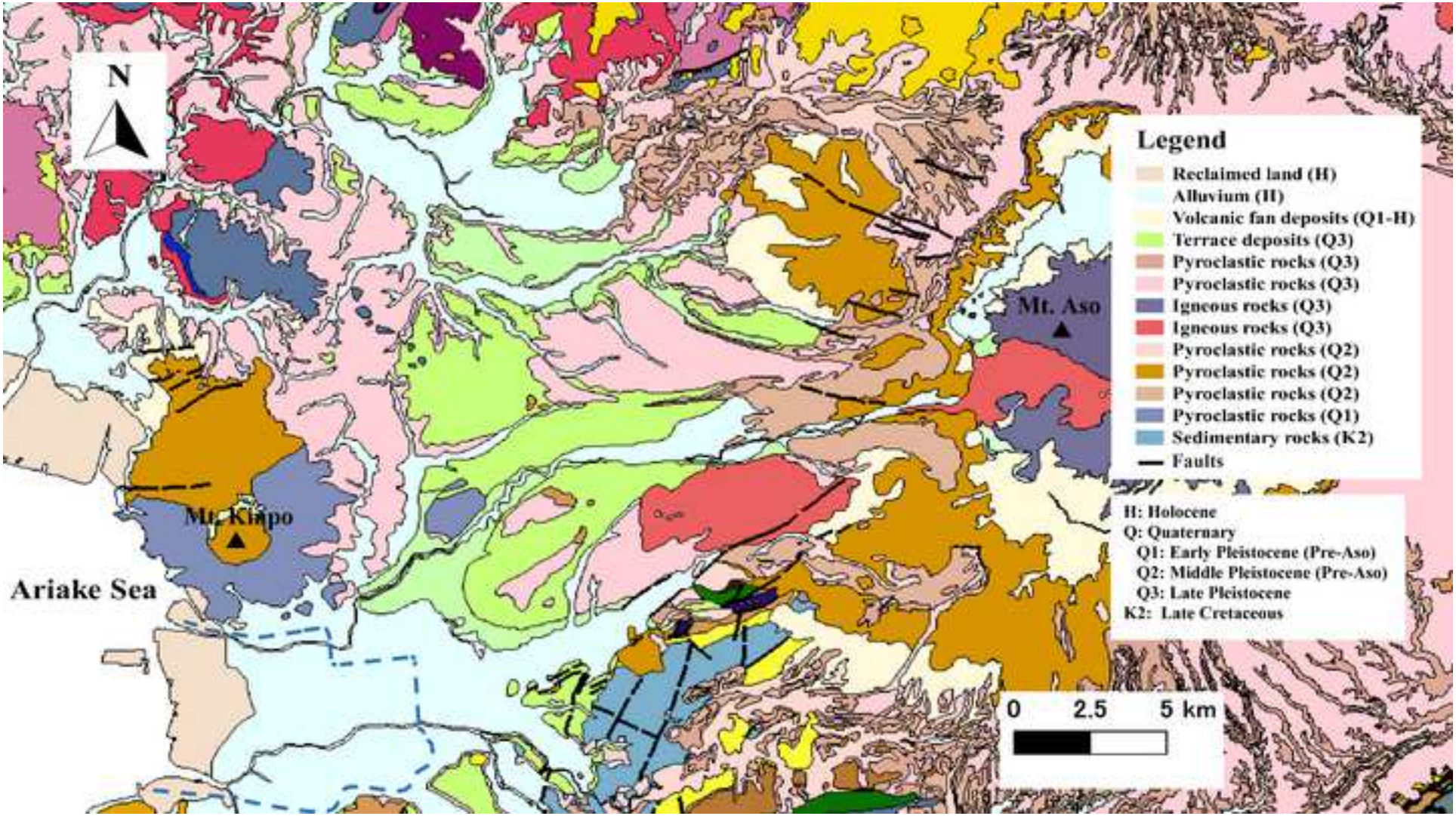

Figure 3

Click here to download high resolution image

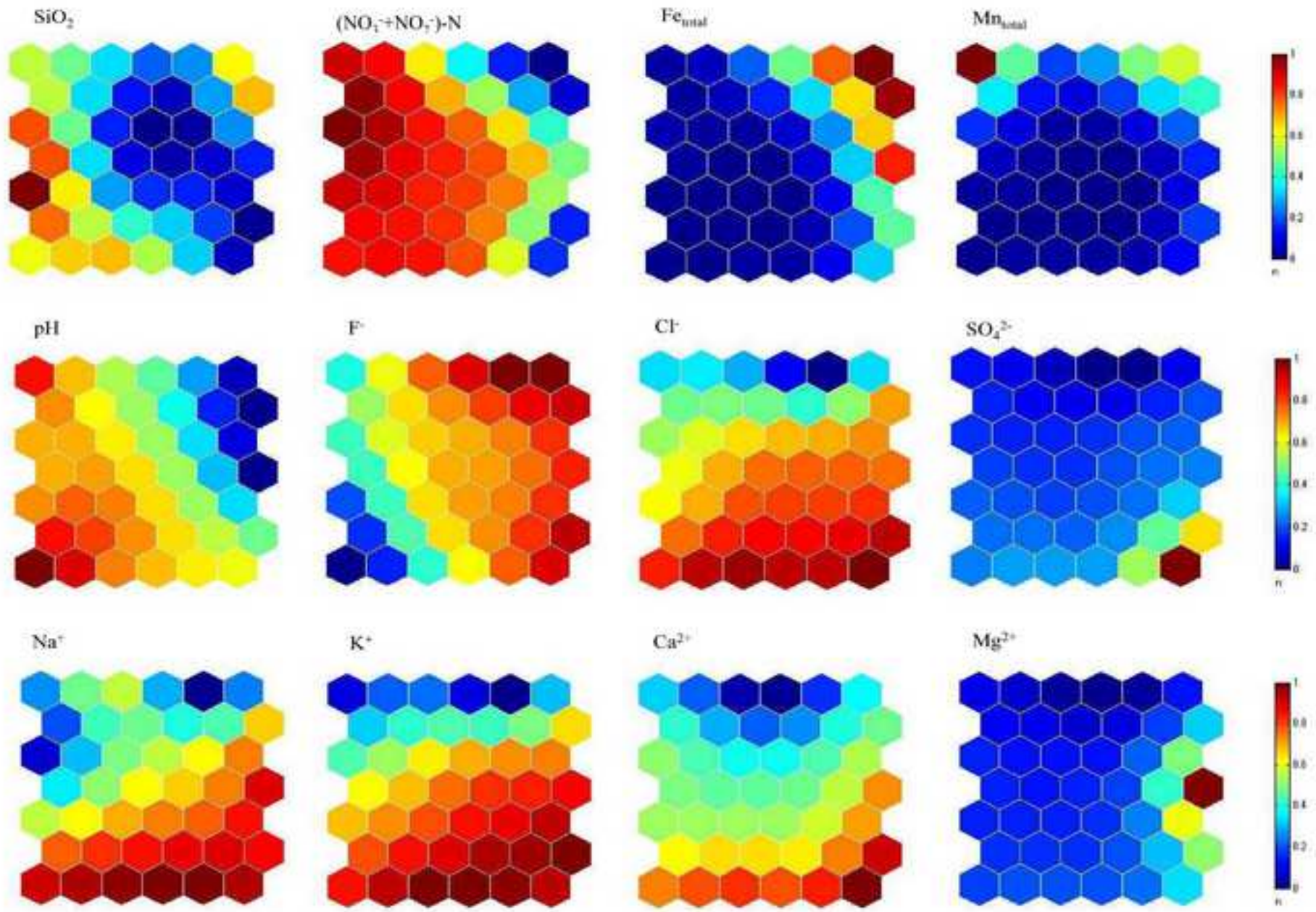

Figure 4
Click here to download high resolution image

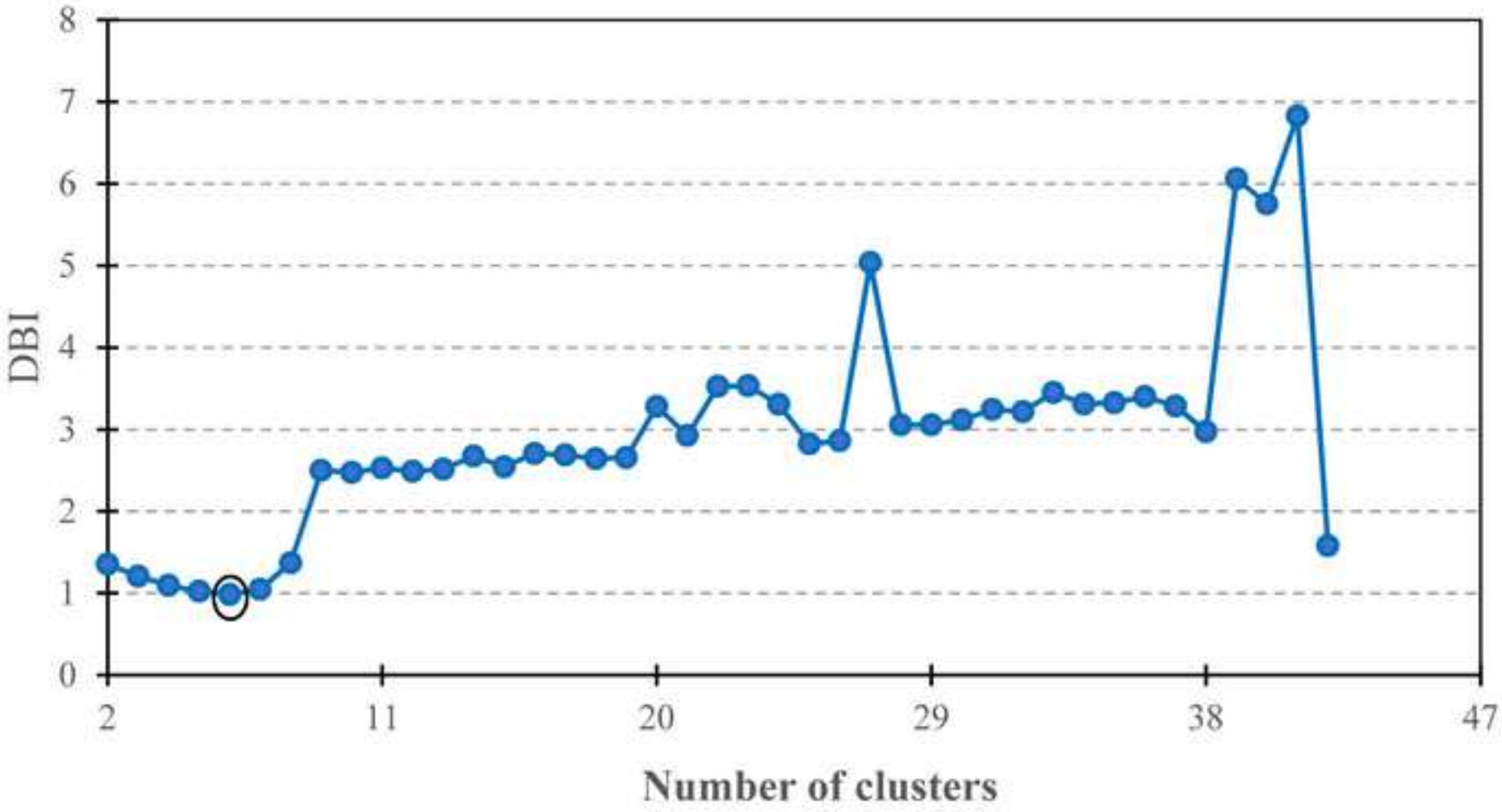

Figure 5
Click here to download high resolution image

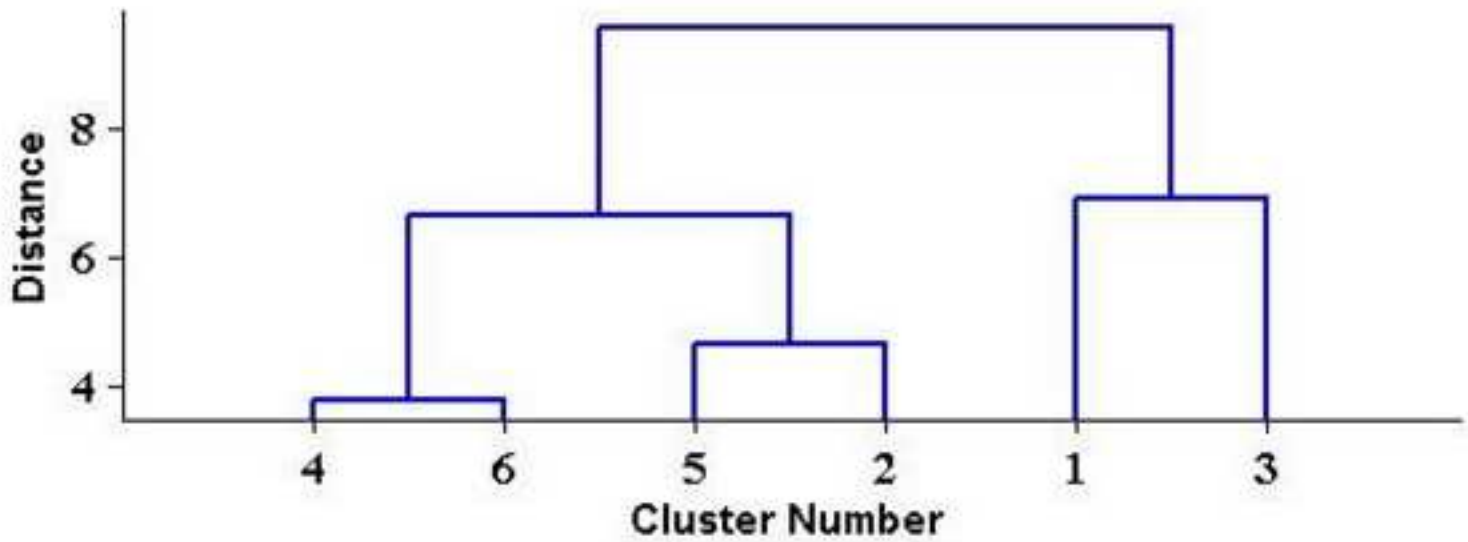

4	6	5	2	1	3
38	41	5	11	1	22
39	42	6	17	2	29
40		7	18	3	30
		12	19	4	36
		13	20	8	37
		14	21	9	
			24	10	
			25	15	
			26	16	
			27	23	
			28		
			31		
			32		
			33		
			34		
			35		

Figure 6
Click here to download high resolution image

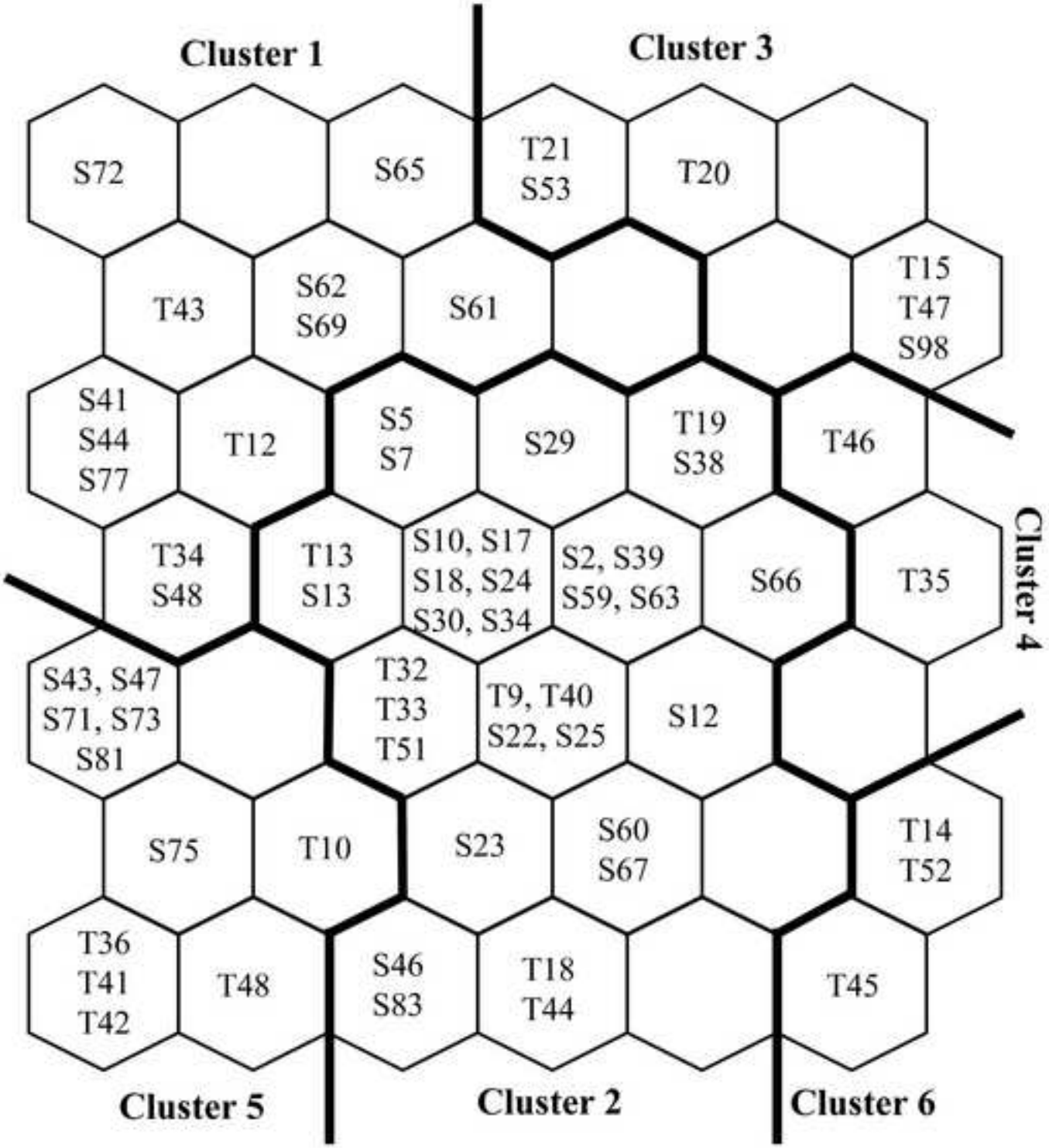

Figure 7

Click here to download high resolution image

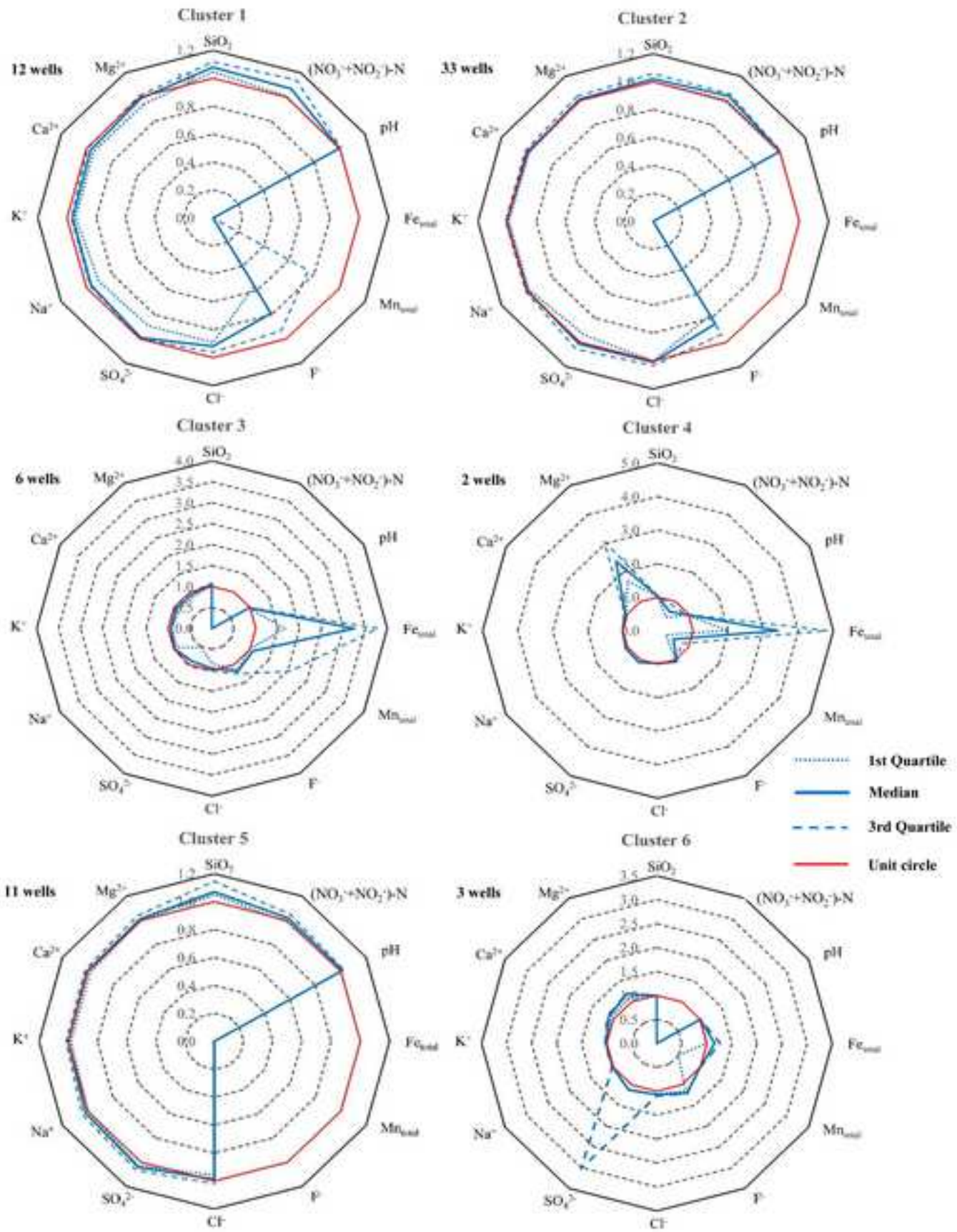

Figure 8
Click here to download high resolution image

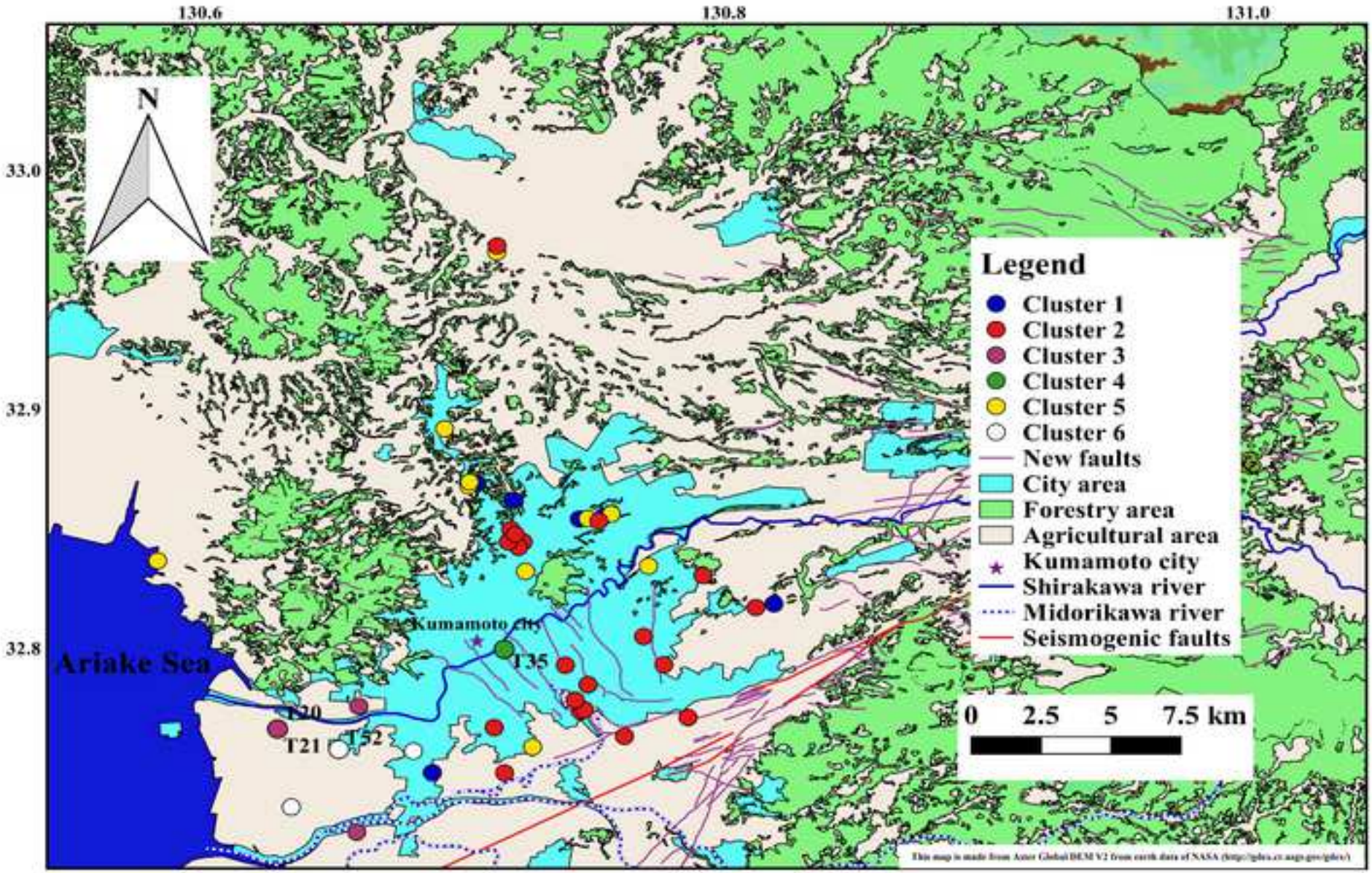

Figure 9
Click here to download high resolution image

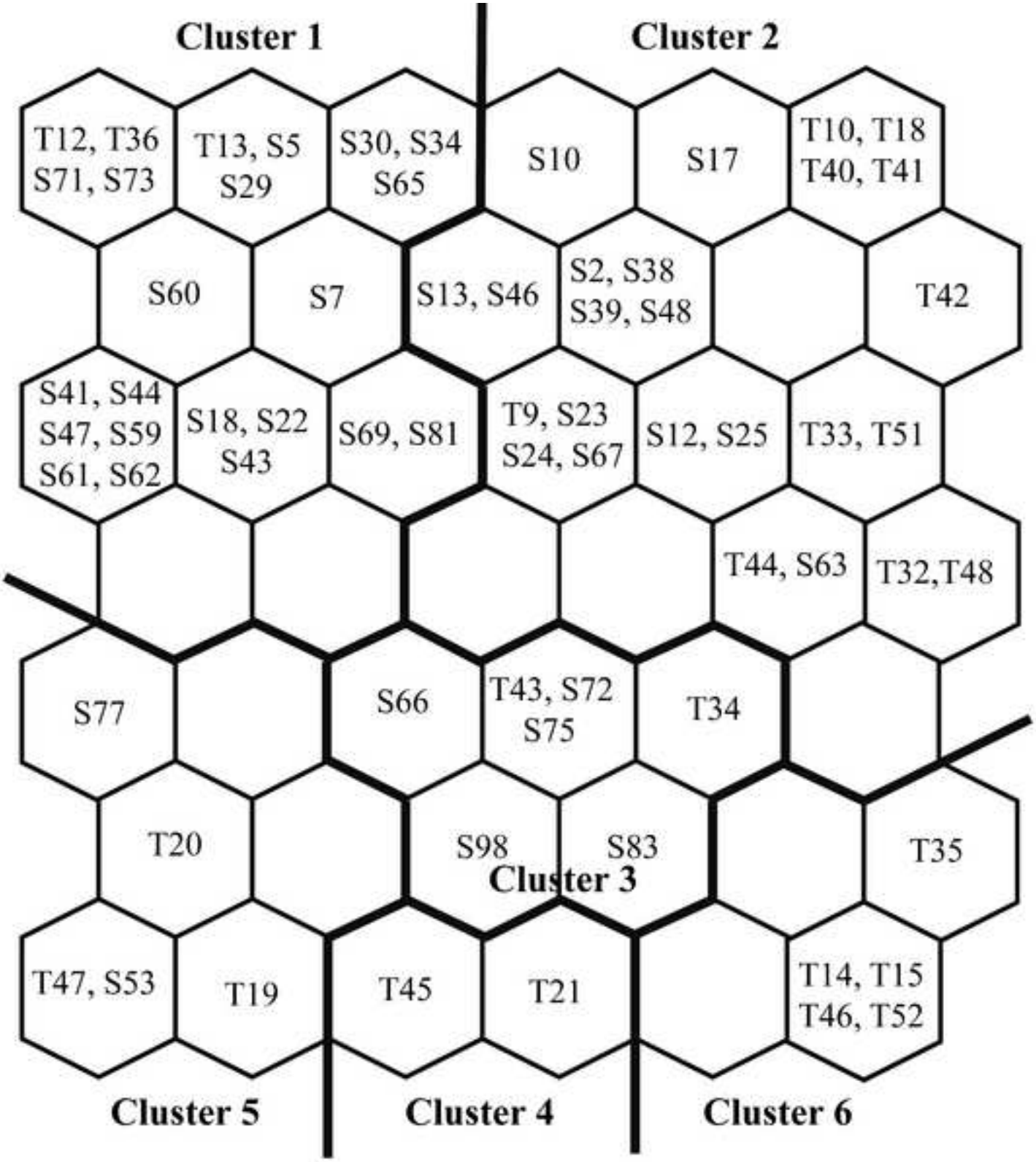

Figure 10

Click here to download high resolution image

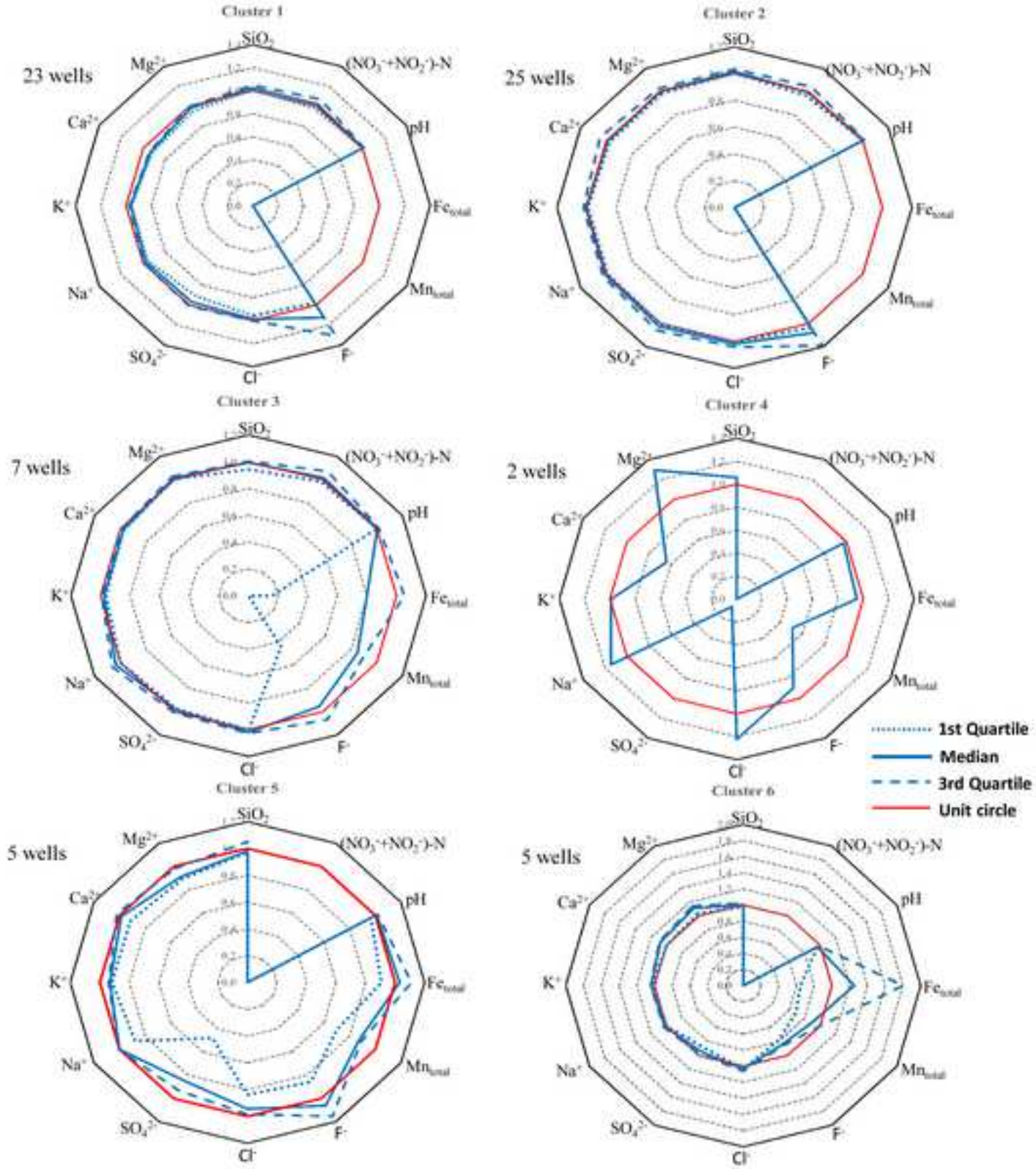

Table 1

ID	Longitude	Latitude	Well depth (m)	Screen depth (m)	Well type	Aquifer type
T9	130.739528	32.792944	55.5	39.00-50.00	deep	confined
T10	130.727028	32.758778	35.3	22.30-33.30	shallow	unconfined
T12	130.819167	32.818611	90.0	60.00-90.00	deep	confined
T13	130.812278	32.817110	70.0	65.00-70.00	deep	confined
T14	130.681528	32.757028	45.7	31.70-42.70	shallow	unconfined
T15	130.681528	32.757028	154.5	121.5-138.0	deep	confined
T18	130.716333	32.747944	41.2	24.70-35.70	shallow	unconfined
T19	130.629667	32.766306	210.0	127.5-149.5	deep	confined
T20	130.629667	32.766306	100.0	53.30-64.30	shallow	unconfined
T21	130.629667	32.766306	15.0	6.75-12.25	shallow	unconfined
T32	130.745333	32.773639	24.8		shallow	unconfined
T33	130.746806	32.774333	25.0		shallow	unconfined
T34	130.716194	32.799611	65.4	39.50-55.40	deep	confined
T35	130.716194	32.799611	21.4	10.40-15.90	shallow	unconfined
T36	130.771278	32.834444	110.0	71.39-93.45	deep	confined
T40	130.777167	32.793167	70.8	48.00-59.00	deep	confined
T41	130.703000	32.869611	60.0	54.00-59.50	shallow	unconfined
T42	130.703000	32.869611	100.0	83.50-94.50	deep	confined
T43	130.712361	32.766861	80.0	36.10-47.10	shallow	unconfined
T44	130.712361	32.766861	115.3	82.32-98.82	deep	confined
T45	130.634917	32.733694	10.0	4.50-10.00	shallow	unconfined
T46	130.634917	32.733694	93.0	57.50-74.00	deep	confined
T47	130.634917	32.733694	145.0	112.0-145.0	deep	confined
T48	130.583889	32.836667	110.1		deep	confined
T51	130.769389	32.804944	137.0	120.5-131.5	deep	confined
T52	130.653056	32.757778	109.0	76.00-92.50	deep	confined
S2	130.743300	32.778280	41.0	35.00-39.00*	deep	confined
S5	130.743300	32.778280	40.0	35.00-39.00*	deep	confined
S7	130.743300	32.778280	60.0	35.00-39.00*	deep	confined
S10	130.743300	32.778280	47.5	35.00-39.00*	deep	confined
S12	130.786380	32.771110	160.0	119.5-125.0*	deep	confined
S13	130.786380	32.771110	140.5	119.5-125.0*	deep	confined
S17	130.786380	32.771110	170.0	119.5-125.0*	deep	confined
S18	130.786380	32.771110	180.0	119.5-125.0*	deep	confined
S22	130.762130	32.763240	201.5	166.0-199.0*	deep	confined
S23	130.762130	32.763240	210.0	166.0-199.0*	deep	confined
S24	130.762130	32.763240	130.0		deep	confined

S25	130.762130	32.763240	200.0	166.0-199.0*	deep	confined
S29	130.748180	32.784810	45.0		deep	confined
S30	130.748180	32.784810	47.2		deep	confined
S34	130.748180	32.784810	51.0		deep	confined
S38	130.792060	32.830570	103.5	84.00-89.00*	deep	confined
S39	130.792060	32.830570	107.4	84.00-89.00*	deep	confined
S41	130.754460	32.855460	123.0	84.00-89.00*	deep	confined
S43	130.757070	32.856260	137.0	113.0-130.0*	deep	confined
S44	130.744900	32.854170	145.0	113.0-130.0*	deep	confined
S46	130.752330	32.853360	120.0	84.00-89.00*	deep	confined
S47	130.748100	32.854320	111.0	84.00-89.00*	deep	confined
S48	130.688760	32.748040	200.0	113.5-124.5*	deep	confined
S53	130.660700	32.775770	125.0	111.5-122.5*	deep	confined
S59	130.723380	32.844530	131.0	110.0-131.0*	deep	confined
S60	130.721690	32.842320	140.0	110.0-131.0*	deep	confined
S61	130.723380	32.844530	7.6		shallow	unconfined
S62	130.721690	32.842320	9.5	3.50-8.50*	shallow	unconfined
S63	130.718700	32.849790	100.0	.	deep	confined
S65	130.718700	32.849790	9.6	3.50-8.50*	shallow	unconfined
S66	130.717760	32.844530	124.0		deep	confined
S67	130.720410	32.847710	127.0		deep	confined
S69	130.724310	32.832250	120.0	75.77-86.84*	deep	confined
S71	130.724310	32.832250	10.0		shallow	unconfined
S72	130.705740	32.868950	212.0		deep	confined
S73	130.702640	32.867956	150.0		deep	confined
S75	130.693440	32.891890	150.0	102.0-107.0*	deep	confined
S77	130.719630	32.862070	152.0		deep	confined
S81	130.713320	32.965810	44.6		deep	confined
S83	130.713480	32.968430	90.0		deep	confined
S98	130.659880	32.723170	206.0		deep	confined

* Denotes reference values of screen depth from close-by water level observation well.
Blank space implies that there are no data.

Table 2

Click here to download Table: 5_Table 2.docx

	Well number	Concentration ratio	Estimated Conc. (2016), (mg/L)	Measured Conc. (2016)*, (mg/L)	Estimated Conc.+2 σ (upper limit), (mg/L)	Estimated Conc.-2 σ (lower limit), (mg/L)
Cluster 1						
SiO_2	S72	1.08	72.5	78	76.0	68.9
	S41	1.12	56.1	63	58.3	53.9
	S44	1.09	55.2	60	57.3	53.2
	S77	1.08	63.1	68	67.0	59.2
	T34	1.17	48.6	57	50.4	46.8
	S48	1.19	55.3	66	59.1	51.4
	S62	1.08	55.6	60	59.3	51.8
	S69	1.12	56.4	63	59.6	53.2
$(NO_3^-+NO_2^-)$-N	S72	0.72	4.50	3.25	5.44	3.56
	T43	1.88	0.39	0.74	0.47	0.32
	S77	1.19	4.89	5.81	5.73	4.06
	T34	2.46	0.14	0.34	0.31	-0.04
	S69	0.94	3.80	3.57	3.87	3.72
Fe_{total}	T43	0.00	0.126	0.00	0.212	0.04
	T34	0.246	0.366	0.09	0.484	0.248
Mn_{total}	S72	8.250	0.008	0.066	0.03	-0.014
F^-	S72	0.00	0.00	0.07	0.00	0.00
	S41	0.00	0.161	0.00	0.245	0.077
	S44	0.408	0.147	0.06	0.177	0.117
	S77	0.619	0.21	0.13	0.275	0.145
	S69	0.617	0.227	0.14	0.292	0.162
Cl^-	S72	0.80	12.41	9.9	13.77	11.05
	S44	0.91	9.00	8.2	9.75	8.25
	S48	0.97	12.59	12.2	12.92	12.26
	S61	0.88	10.49	9.2	11.50	9.48
	S62	0.90	11.48	10.3	12.54	10.42
	S69	0.96	10.0	9.6	10.18	9.82
	S65	0.79	25.43	20.1	27.69	23.17
SO_4^{2-}	S61	0.89	8.64	7.7	9.23	8.05
	S65	0.65	12.79	8.3	16.67	8.91
Na^+	T43	0.95	20.0	19.0	20.0	20.0
	S41	0.82	15.47	12.7	17.86	13.08
	S44	0.85	17.42	14.8	19.61	15.23

	S65	1.10	27.33	30.0	28.77	25.89
K^+	T43	0.94	7.66	7.20	7.77	7.55
Ca^{2+}	S72	0.89	16.11	14.3	17.28	14.94
	S77	1.08	21.17	22.9	22.87	19.47
	S69	0.95	18.73	17.8	19.52	17.94
	S65	0.81	19.49	15.8	21.95	17.03
Mg^{2+}	S77	1.12	7.29	8.2	8.03	6.55
	T34	1.08	13.90	15.0	14.79	13.01
	S65	0.83	6.59	5.5	7.30	5.88
Cluster 2						
SiO_2	T18	1.05	55	58	56.10	53.90
	T19	0.82	21.9	18	25.19	18.61
	T32	1.06	55.8	59	56.69	54.91
	T40	1.02	54.8	56	55.69	53.91
	T44	1.04	71.1	74	72.77	69.43
	S13	1.06	55.68	59	57.85	53.51
	S22	1.05	54.51	57	56.18	52.84
	S23	1.15	54.03	62	57.05	51.01
	S38	1.07	53.97	58	54.58	53.36
	S39	1.09	53.36	58	54.59	52.13
	S46	1.14	55.2	63	56.90	53.50
	S60	1.09	65.89	72	68.52	63.26
	S67	1.07	65.5	70	68.47	62.53
	S83	1.20	67.72	81	72.42	63.02
$(NO_3^-+NO_2^-)$-N	T51	0.90	3.66	3.3	3.77	3.55
	S5	1.06	3.398	3.6	3.59	3.20
	S7	1.04	3.464	3.61	3.58	3.34
	S10	1.05	3.324	3.48	3.46	3.19
	S17	1.04	2.197	2.29	2.25	2.14
	S22	1.05	2.269	2.38	2.32	2.22
	S24	1.07	2.39	2.56	2.45	2.33
	S25	1.05	2.223	2.34	2.29	2.15
	S29	1.06	3.475	3.67	3.65	3.30
	S34	1.05	3.592	3.78	3.77	3.41
	S46	1.12	4.816	5.41	5.33	4.30
	S59	0.80	0.758	0.61	0.79	0.73
	S60	0.71	0.678	0.48	0.73	0.63

Fe_{total}	S63	0.00	0.00	0.04	0.00	0.00
Mn_{total}	S63	0	0	0.008	0	0
pH	T51	1.03	7.09	7.30	7.18	7.00
	S23	1.01	7.10	7.20	7.10	7.10
	S38	0.97	7.22	7.0	7.36	7.08
	S39	0.98	7.13	7.0	7.24	7.02
	S83	0.99	7.20	7.1	7.20	7.20
F^-	S2	0.78	0.193	0.15	0.22	0.17
	S5	0.75	0.187	0.14	0.20	0.17
	S7	0.86	0.174	0.15	0.18	0.16
	S10	0.85	0.177	0.15	0.20	0.16
	S12	0.77	0.207	0.16	0.22	0.19
	S13	0.80	0.226	0.18	0.25	0.20
	S17	0.76	0.237	0.18	0.25	0.22
	S18	0.73	0.219	0.16	0.25	0.19
	S22	0.87	0.23	0.2	0.25	0.21
	S23	1.19	0.219	0.26	0.23	0.21
	S24	0.83	0.24	0.2	0.26	0.22
	S29	0.83	0.181	0.15	0.20	0.16
	S30	0.83	0.18	0.15	0.20	0.16
	S34	0.79	0.177	0.14	0.19	0.16
	S46	0.00	0.089	0.00	0.13	0.05
	S59	0.88	0.855	0.75	0.92	0.79
	S67	0.92	0.793	0.73	0.83	0.76
	S83	0.00	0.095	0.00	0.13	0.06
Cl^-	T40	1.01	9.28	9.4	9.39	9.17
	S13	0.99	8.01	7.9	8.10	7.92
	S17	1.03	8.37	8.6	8.51	8.23
	S22	1.04	8.78	9.1	8.89	8.67
	S23	1.03	9.04	9.3	9.15	8.93
	S24	1.05	8.8	9.2	8.98	8.62
	S38	0.96	9.75	9.4	10.02	9.48
	S46	1.13	8.12	9.2	8.70	7.54
	S60	1.08	30.97	33.3	31.35	30.59
	S83	1.08	4.27	4.6	4.50	4.04
SO_4^{2-}	T9	1.08	19.4	21	20.81	17.99
	S12	1.04	32.58	33.8	33.45	31.71
	S13	1.02	31	31.6	31.39	30.61

	S17	1.03	34.13	35	34.89	33.37
	S18	1.03	31.21	32.3	31.61	30.81
	S25	0.98	34.44	33.6	35.22	33.66
	S67	1.04	6.52	6.8	6.70	6.34
Ca^{2+}	T19	0.94	8.18	7.7	8.36	8.0
	S83	1.08	8.72	9.4	9.37	8.07
Mg^{2+}	T19	0.89	3.84	3.4	4.08	3.60
	T51	0.97	7.86	7.6	7.97	7.75
	S10	1.09	8.16	8.9	8.87	7.45
	S18	1.05	8.64	9.1	8.94	8.34
	S59	1.04	5.6	5.8	5.60	5.60
	S83	1.07	4.47	4.8	4.74	4.20
Cluster 3						
SiO_2	S53	1.09	58.8	64	61.5	56.1
	S98	1.26	46.9	59	50.9	42.9
Fe_{total}	T20	3.64	0.33	1.2	0.59	0.07
	S53	2.86	0.063	0.18	0.17	-0.04
	T15	3.85	0.078	0.3	0.14	0.01
	T47	3.84	0.099	0.38	0.19	0.01
Mn_{total}	T20	4.211	0.038	0.16	0.062	0.014
	T21	0.769	0.078	0.06	0.095	0.061
	T15	2.368	0.038	0.09	0.056	0.02
pH	S98	0.98	7.72	7.60	7.83	7.61
F^-	T20	1.69	0.767	1.3	1.07	0.46
Cl^-	T20	0.39	113.2	44	147.2	79.2
	T21	0.81	135	110	156.9	113.1
	S53	0.91	27.03	24.7	29.33	24.73
SO_4^{2-}	T15	1.09	22	24	22.0	22.0
Na^+	T20	0.69	160	110	184.5	135.5
K^+	T20	0.80	8.38	6.7	9.45	7.31
Cluster 4						
SiO_2	T46	1.06	38.8	41	40.59	37.01
Fe_{total}	T35	6.25	0.024	0.15	0.051	-0.003
pH	T35	0.93	9.607	8.9	10.14	9.07
Mg^{2+}	T35	3.75	0.56	2.1	0.82	0.30
Cluster 5						

SiO_2	S43	1.15	53.91	62	56.25	51.57
	S47	1.20	54.97	66	57.94	52.0
	S71	1.14	52.59	60	54.97	50.21
	S73	1.09	73.72	80	77.04	70.40
	S81	1.16	72.36	84	75.52	69.20
	T36	1.04	52	54	53.10	50.90
	T41	1.04	71.1	74	72.77	69.43
	T42	1.07	73.8	79	76.25	71.35
	T10	1.06	58.6	62	59.70	57.50
$(NO_3^-+NO_2^-)$-N	T42	1.05	4.78	5.0	4.95	4.61
	T48	1.26	1.43	1.8	1.69	1.17
Cl^-	S71	0.94	9.49	8.9	9.87	9.11
	S73	0.89	10.85	9.7	11.11	10.59
	S81	0.93	7.82	7.3	8.02	7.62
	T48	1.19	5.73	6.8	6.44	5.02
SO_4^{2-}	S43	1.10	6.01	6.6	6.15	5.87
	S47	1.06	6.42	6.8	6.72	6.12
	S71	1.08	9.86	10.6	10.30	9.42
	T48	1.49	3.9	5.8	4.40	3.40
Ca^{2+}	T36	1.17	13.7	16	14.80	12.60
Mg^{2+}	T42	1.05	5.72	6	5.86	5.58
	T48	1.09	4.75	5.2	5.16	4.34
	S81	0.98	6.74	6.60	6.83	6.65
Cluster 6						
F^-	T52	1.20	0.36	0.43	0.42	0.30
SO_4^{2-}	T14	1.13	36.40	41.0	39.08	33.72
	T45	4.92	0.13	0.62	0.34	-0.09
	T52	1.10	22.80	25.0	24.21	21.39
Mg^{2+}	T52	1.19	1.26	1.50	1.48	1.04

*The red color data represent the 2016 year`s measured concentration which is larger than the upper limit, on the contrary, the blue color data is smaller than the lower limit.